HTML ABSTRACT + LINKS

Numerical investigations of flow over a sphere in the subcritical and supercritical regimes

George Constantinescu[a)]
Civil and Environmental Engineering Department, The University of Iowa, Iowa City, Iowa 52242

Kyle Squires
Mechanical and Aerospace Engineering Department, Arizona State University, Tempe, Arizona 85287-6016

(Received 10 September 2003; accepted 29 January 2004; published online 5 April 2004)

The flow field around a sphere in an uniform flow has been analyzed numerically for conditions corresponding to the subcritical (laminar separation) and supercritical (turbulent separation) regimes spanning a wide range of Reynolds numbers (10^4–10^6). Particular attention has been devoted to assessing predictions of the pressure distribution, skin friction, and drag as well as to understanding the changes in the wake organization and vortex dynamics with the Reynolds number. The unsteady turbulent flow is computed using detached-eddy simulation, a hybrid approach that has Reynolds-averaged Navier–Stokes behavior near the wall and becomes a large eddy simulation in the regions away from solid surfaces. For both the subcritical and supercritical solutions, the agreement with experimental measurements for the mean drag and pressure distribution over the sphere is adequate; differences in skin friction exist due to the simplistic treatment of the attached boundary layers in the computations. Improved agreement in the skin-friction distribution is obtained for the supercritical flows in which boundary layer transition is fixed at the position observed in experiments conducted at the same Reynolds numbers. For the subcritical flows the Strouhal number, St, associated with the large-scale shedding is predicted at St$\sim$0.195 along with a higher frequency component associated with the development of the Kelvin–Helmholtz instabilities in the detached shear layers. If in the subcritical regime the wake assumes a helical-like form due to the shedding of hairpin-like vortices at different azimuthal angles, in the supercritical regime the wake structure is characterized by ''regular'' shedding of hairpin-like vortices at approximately the same azimuthal angle and at a much higher frequency (St$\sim$1.3) that is practically independent of the Reynolds number and not sensitive to the position of laminar-to-turbulent transition. © *2004 American Institute of Physics.* [DOI: 10.1063/1.1688325]

I. INTRODUCTION

Prediction of flows that exhibit massive separation remains one of the principal challenges to computational fluid dynamics (CFD). The main interest of the present study is calculation of the turbulent flow over a sphere at high Reynolds numbers. Perhaps the most well known feature of the flow over a sphere is the occurrence of the drag crisis around a critical Reynolds number of $Re_{cr}=3.7*10^5$, a manifestation of the significant differences between laminar and turbulent boundary layer separation. While the geometry is simple, the flow field that develops around the sphere is complex, possessing many of the aspects that are difficult to accurately capture in numerical models, e.g., transition from laminar to turbulent flow, massive separation, large-scale vortex shedding in the turbulent wake, etc. Flow field predictions in this work are obtained using detached-eddy simulation (DES), a hybrid technique which essentially reduces to a Reynolds-averaged Navier–Stokes (RANS) treatment near the walls and becomes a large eddy simulation (LES) in the regions away from solid surfaces, provided the grid density is sufficient.[1,2] DES is a nonzonal technique that is computationally feasible for high Reynolds number predictions, but also resolves time-dependent, three-dimensional turbulent motions as in LES. Previous applications of the method have been favorable, yielding adequate predictions across a wide range of flows (e.g., see Strelets[3] and references therein) and also showing that the computational cost has a weak dependence on Reynolds number, similar to RANS methods, yet at the same time providing more realistic descriptions of unsteady effects. In this work, DES is applied to prediction of the flow around a sphere for both subcritical (laminar boundary layer separation; transition to turbulence occurs in the separated shear layers) and supercritical (turbulent boundary layer separation) regimes. The goal is to assess the accuracy of the modeling approach in predicting quantities such as the skin-friction and pressure distributions around the sphere and, related, the drag and side forces. Additionally, an important aim of the work is to assess the time-dependent features of the solutions and the changes in the wake structure with Reynolds number.

As also true for the circular cylinder, the sphere is known for its drag crisis, a reflection of the substantial differences in separation of laminar and turbulent boundary lay-

[a)]Telephone: 319 384 0630; electronic mail: sconstan@engineering.uiowa.edu

 © 2004 American Institute of Physics

Downloaded 19 Jul 2004 to 195.83.232.39. Redistribution subject to AIP license or copyright, see http://pof.aip.org/pof/copyright.jsp

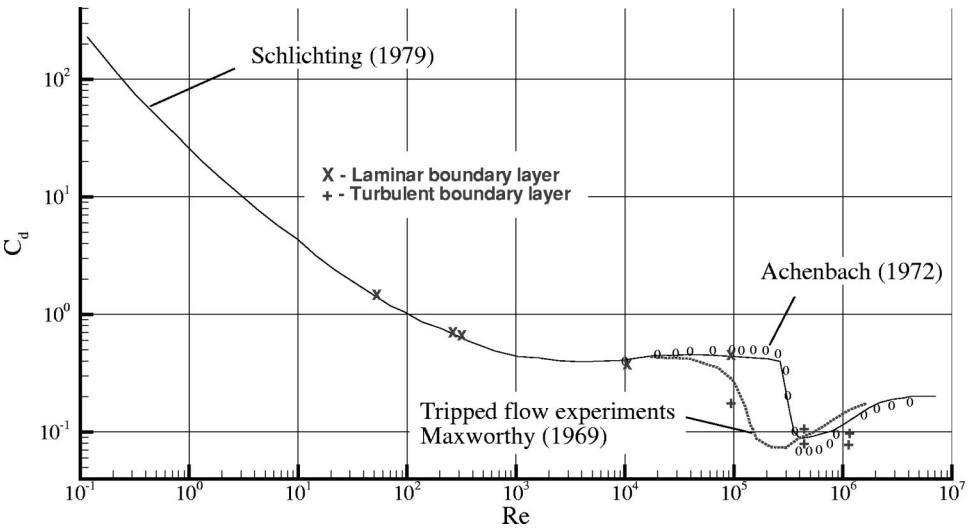

FIG. 1. Drag coefficient for uniform flow over a sphere as a function of the Reynolds number. Experimental data from Schlichting (1979), Achenbach (1972), and Maxworthy (1969).

ers. Consequently, construction of the simulation and especially the boundary layer treatment within a computation is important. The simulation design employed in this effort parallels in many respects the earlier calculations of the circular cylinder by Travin *et al.*[2] Both in this contribution and in the cylinder simulations the boundary layer treatment of the subcritical flow is the same. Relevant to the present application is the previous work[4] on the subcritical flow over a sphere at $\mathrm{Re}=10^4$, in which DES predictions of the flow past a sphere were adequate based on comparison to experimental measurements,[5] as well as to LES results obtained using a dynamic subgrid model.

Prediction of flows in the supercritical regime increases the burden on the model, primarily through the need to predict boundary layer growth and separation, which is under the control of a RANS model in natural DES applications. This increase in the empirical content of the modeling approach appears unavoidable—the cost of whole-domain LES in the supercritical regime is not far from that of direct numerical simulation because of the resolution needed to capture the turbulence structures (e.g., streaks) inside the thin attached turbulent boundary layers. Even with wall-layer models, the computational cost of LES applied to high Reynolds number flows is not small and, in addition, wall-layer modeling remains a topic of considerable fundamental interest for which new modeling strategies are being actively pursued.[6,7] Analogous to the cylinder, in the supercritical regime the attached boundary layers along the sphere become turbulent prior to flow detachment and the details of the transition process are complex. In the work reported below, a simple treatment of the boundary layers is applied in most cases (fully turbulent from the stagnation point), an approach that leads to differences compared to measurements in prediction of the skin friction. Because of these differences, some computations were also performed to investigate the influence of laminar-to-turbulent transition by fixing the position at which the turbulence model becomes active at a position closer to where transition is observed in experiments. One of the contributions of the present manuscript is an opportunity to evaluate the simulation methodology as applied to a canonical configuration by comparing not only the prediction of integrated quantities, such as the drag, but also the time-dependent features of the shedding process. This work also allows us to gain some insight into the degree to which well-defined, though simple, treatments of the attached boundary layers influence the predictions.

For Reynolds numbers below the critical value, $\mathrm{Re}_{\mathrm{cr}}$, it is possible in experiments to trip the flow in order to induce transition to turbulence of the attached boundary layer prior to the location where eddies are detaching from the sphere surface. Similarly, for supercritical flows it is possible to induce earlier transition of the attached boundary layers than occurs naturally in "quiet" conditions, by tripping the boundary layers upstream of the location corresponding to natural transition. Maxworthy,[8] for example, attached a thin circular wire at a constant polar angle, $\varphi=55°$ (the origin corresponding to the upstream stagnation point), on the sphere. Drag measurements from the experimental investigation of Maxworthy[8] are represented with a dotted line in Fig. 1 along with the classical curve $C_d=C_d(\mathrm{Re})$ for the flow over a sphere.[9] Thus, over a range of Reynolds numbers ($\mathrm{Re}<\mathrm{Re}_{\mathrm{cr}}$), two distinct wake configurations are possible, corresponding to either a laminar boundary separation or a turbulent boundary layer separation. This is exemplified in Fig. 1 and Table I, by the two calculations at $\mathrm{Re}=10^5$, one (subcritical) which is very close to the drag value given by Schlichting,[9] as expected, and one (supercritical) which yields a lower drag (transition was imposed at $\varphi=0°$).

Presented in the next subsection is a summary of some of the features of the flow over a sphere based on experimental investigations and a discussion of the previous numerical investigation of the flow past spheres. Following is then an overview of the computational approach with a description of the numerical method. Results from the computations are presented along with a summary of the findings from this effort.

II. BACKGROUND

The flow past spheres has been documented mostly using lab experiments for several years with many studies con-

Downloaded 19 Jul 2004 to 195.83.232.39. Redistribution subject to AIP license or copyright, see http://pof.aip.org/pof/copyright.jsp

TABLE I. Effect of Reynolds number and flow conditions on flow parameters. (s)—subcritical regime; (S)—supercritical regime; (ft)—fully turbulent boundary layers. Experimental measurements from Achenbach (1972).

Re	C_d	C_d expt.	$C_\tau/C_d(\%)$	$C_\tau/C_d(\%)$ expt.	φ_s	φ_s expt.	φ_t	φ_t expt.
300	0.655 ± 0.0032	0.63	42	⋯	111	113	⋯	⋯
10^4(s)	0.393 ± 0.009	0.4	8.3	5.5	84 ± 1	82.5	101	⋯
10^5(s)	0.414 ± 0.026	0.4–0.5	2.2	1.8	81.5 ± 1	82.5	90	⋯
10^5(S)(ft)	0.191 ± 0.012	⋯	10.2	⋯	103 ± 2	⋯	0	⋯
$4.2*10^5$(S)	0.093 ± 0.010	0.085	13.1	13.0	118 ± 2	119	100	98
$4.2*10^5$(S)(ft)	0.117 ± 0.0096	⋯	15.2	⋯	114 ± 2	⋯	0	⋯
$1.14*10^6$(S)	0.080 ± 0.0075	0.12	12.1	7.5	120 ± 2	120	98	98
$1.14*10^6$(S)(ft)	0.102 ± 0.011	⋯	15.2	⋯	117 ± 2	⋯	0	⋯

centrating on qualitatively describing the flow using visualization techniques. Several quantitative measurements of the flow over a sphere have been reported.[5,10–12] These investigations were mostly interested in documenting the different flow regimes, studying the changes in the wake structure and shedding mechanism with the Reynolds number, and proposing models for the vortical structure of the wake. With the exception of a recent investigation[13] of the flow past spheres in the subcritical regime at $\mathrm{Re}=5*10^4$, none of these investigations contained detailed measurements of the near-wake properties at subcritical or supercritical conditions that would enable a detailed study of the vortical structures in the wake and a full validation of the CFD calculations.

These previous works have shown that the topology and shedding process around the sphere vary significantly with Reynolds number. Experimental investigations have shown that for $\mathrm{Re}>270-300$ ($\mathrm{Re}>400$ according to Refs. 14 and 15), a spiral instability mode is present. This mode is related to the large-scale (sinuous) instability of the wake and is due to the coherent rotation of the recirculation zone, and consequently of the separation line on the sphere. This instability manifests as a progressive wave motion with alternate fluctuations produced by the shear present at the limit between the recirculation zone and the exterior fluid. The alternate fluctuations determine the periodic shedding of hairpin-shaped vortices from the sphere to form a completely laminar wake. Most of the large-scale vorticity of the shed structures originates from the separation of the shear layers at the sphere surface. This mode is associated with the large-scale vortex shedding in the laminar and subcritical regimes. Between $\mathrm{Re}=300$ and $\mathrm{Re}=800$, laminar hairpin-like vortices are shed behind the sphere. A new instability that manifests as an axisymmetric shedding of vortex tubes due to pulsations in the separated shear layer is present[14] starting at $\mathrm{Re}=800$. The observed threshold value ($\mathrm{Re}=800$) agrees very well with the one determined in other experiments.[11,15] This last mode is associated with the small-scale shear-layer Kelvin–Helmholtz instability on the periphery of the recirculation region, and is responsible for the distortion of the large-vortex structures, shedding of the vortex tubes in a quasi-coherent fashion, production of small scales and, eventually, transition to turbulence in the detached shear layers. Bakic[13] was able to capture in his visualizations the roll up and pairing processes that accompany transition to turbulence of the vortex tubes. Experiments clearly show that the two instability modes co-exist simultaneously up to a certain Reynolds number in the subcritical regime. However, there is some disagreement on this particular value of the Reynolds number. Achenbach[15] did not detect the high frequency mode beyond $\mathrm{Re}=6000$, Sakamoto and Haniu[12] failed to capture it beyond $\mathrm{Re}=1.5*10^4$, while in some experiments[11,13] the presence of the two modes was detected up to $\mathrm{Re}\sim10^5$. The energy content of the high frequency mode is relatively high in the detached shear layers.

There is better agreement on the values of the frequencies (expressed in nondimensional form as a Strouhal number) associated with these two modes in the subcritical regime. The Strouhal number which corresponds to the shedding (spiral) mode remains approximately constant at 0.18–0.2 (depending on the investigation[15,16]) for $\mathrm{Re}>6000$ when the transition to turbulence of the separated vortex sheet is completed. The vortex tubes shed from the separation region stabilize and there is a return to a more regular shedding pattern of the large-scale vortices from the formation region up to Reynolds numbers close to the drag crisis ($\sim10^5$). The structure of the large vortices shed in the wake, though not very clear in experiments (as for $\mathrm{Re}>1000$ the vortex loops are known to diffuse very rapidly), seems to maintain a hairpin-shaped form similar to the one observed at lower Reynolds numbers. Experiments[13] confirmed that there is little change in the wake structure and nondimensional parameters in this range. The Strouhal number corresponding to the Kelvin–Helmholtz instability is increasing with the Reynolds number ($\mathrm{Re}>800$) mainly because the shear layers become unstable to smaller wavelengths.

The transition from the subcritical to supercritical regime is accompanied by development of a more compact recirculating region (the length of the primarily recirculation zone is decreasing) in the near wake. The drag coefficient drops from values near 0.4–0.5 prior to the drag crisis to around $C_d=0.07-0.09$.[5,9] In addition to Achenbach,[5] the flow over the sphere in the supercritical regime was investigated experimentally by Taneda[10] who proposed a wake model in which the vortex sheet separating from the sphere rolls up into an Ω-shaped structure to form a pair of coherent streamwise vortices. Based on visualizations, Taneda[10] did

Downloaded 19 Jul 2004 to 195.83.232.39. Redistribution subject to AIP license or copyright, see http://pof.aip.org/pof/copyright.jsp

not observe periodic shedding similar to the one present at subcritical conditions. This change in the wake structure induces a lateral force on the sphere that tilts the wake relative to the streamwise axis. As described in the Results section, the present simulations confirm the presence of such a lateral force and, consequently, the tilting of the wake, but also the shedding of hairpin-like structures at a relatively high frequency ($St \sim 1.3$), considerably larger than the one associated with large-scale vortex shedding in the subcritical regime ($St \sim 0.19$). The main features of the flow remain unchanged up to $Re = 1.5*10^6$.

III. NUMERICAL INVESTIGATIONS

Most of the past numerical investigation of the flow past spheres have focused on investigating the flow in the laminar steady and unsteady regimes, determining the onset of vortex shedding and studying some of the flow features at relatively higher Reynolds numbers (before transition to turbulence occurs in the wake) when the coherent structures shed in the wake become less regular.

Most numerical investigations in the laminar steady and unsteady regimes used either finite-differences methods[17–19] or finite-element approaches.[20–22] In all these simulations the maximum Reynolds number was around $Re = 500$. The flow configuration was not always the same, for instance in Shirayama[17] the sphere was accelerated to the final velocity from rest, and in some of the calculations of Shen and Loc[19] the sphere was allowed to spin and the effect of the Magnus force on the rotating sphere was quantified. However, most of the investigations focused on the flow over a fixed sphere in a freestream. The numerical methods to solve the Navier–Stokes equations in these studies also varied widely from author to author. They included using fractional step algorithms with double time-stepping (Runge–Kutta with multigrid or alternate direciton implicit were used to integrate the equations in pseudo-time), using the velocity-vorticity form of the Navier–Stokes equations and semi-implicit algorithms for discretization, using the Galerkin method in the context of finite elements or solving the compressible Navier–Stokes equations at low Mach numbers. The results from these investigations sometimes performed at exactly the same Reynolds number did not always agree, showing that differences in the numerical methods can affect the results even in the absence of resolved turbulent structures. For instance, the range over which the onset of vortex shedding was observed in these studies varies from 270 to 400, while experimental measurements show a much narrower range of 270–300. Very accurate algorithms[23–25] based on a Fourier–Chebyshev spectral-collocation method were used to simulate flow past spheres and spheroids for Reynolds numbers up to 650 with and without external periodic forcing. The periodic forcing was produced by introducing perturbations in the surrounding flow and was used to study the vortex shedding lock-on phenomenon, where the vortex shedding can lock-on to an external forcing frequency different from the natural shedding frequency.

Some of the numerical investigations also studied the onset of the irregular vortex shedding mode, experimentally determined at $Re = 420$. For instance, the DNS results of Tomboulides *et al.*[26] and Tomboulides and Orszag[27] using a numerical method based on a spectral element-Fourier algorithm showed that the wake structure at $Re = 500$ consists of a succession of interconnected vortex loops. The vortical pattern was similar to that obtained at $Re = 300$ (regular unsteady shedding regime), but the planar symmetry (solution is symmetrical in the plane of zero lateral force) present in the latter was lost. Tomboulides *et al.*[26] did not detect any small-scale turbulence in the wake in the simulation at $Re = 500$. As the Reynolds number was increased to $Re = 1000$, their DNS calculation showed that the shear layers became unstable after separation and small-scale turbulence structures were present in the wake. The Strouhal number associated with the spiral mode assumed a value of 0.202, while the one associated with the Kelvin–Helmholtz instability was close to 0.36. Both values agree well with the ones reported in experiments.[12] The simulation also showed the broadening of the velocity spectrum in the wake, corresponding to the transition to turbulence.

There are relatively few time-accurate simulations in the turbulent regime. Simulations performed in the subcritical regime include the LES of Tomboulides *et al.*[26] at $Re = 2*10^4$ in which a subgrid model based on renormalization group theory was used. They reported values of the Strouhal numbers associated with the two instability modes within 10% of the experimental values;[11] the shedding frequency was 0.2, while the shear-layer frequency was around 3.5. Kim and Choi[28] used LES and an immersed boundary method in cylindrical coordinates in which a hybrid discretization for the convective terms (upwind differences in the region of laminar accelerating flow, central differences elsewhere) was used to calculate the flow past spheres between $Re = 3.7*10^3$ and $Re = 10^4$. The quantitative agreement at the lower Reynolds number with the experimental data[11] (velocity profiles in the wake) was good, while the predictions of the drag coefficient, mean base pressure coefficient and shedding frequency were within the experimental range at both Reynolds numbers. Seidl *et al.*[29] performed DNS at a Reynolds number of 5000. Their simulation was able to correctly predict the formation of the initially laminar vortex tubes in the detached shear layers, as well as the subsequent roll-up, pairing and transition of these vortices. They obtained good agreement for global parameters, such as the streamwise drag, the Strouhal number, etc. Recently, Schmid[30] performed several simulations at $Re = 5*10^4$ using different subgrid stress (SGS) models (Smagorinsky, dynamic and no model). He used a finite volume method and local grid refinement in the detached shear layers to accurately capture the formation of the vortex tubes and their subsequent evolution. The influence of the SGS model used on the mean flow quantities appeared to be rather minor. Subsequently, the results[30] were compared with experiments[13] and overall a good agreement with the experimental data (that included mean velocity and turbulent fluctuations profiles in the wake) collected at the same Reynolds number was observed. This was in contrast with the RANS calculations[31] for the same flow where the agreement was poor not only for the integral

Downloaded 19 Jul 2004 to 195.83.232.39. Redistribution subject to AIP license or copyright, see http://pof.aip.org/pof/copyright.jsp

quantities but also for the wake characteristics. Steady RANS calculations in the subcritical and supercritical regimes were reported by Drikakis[32] who used an artificial compressibility solver in conjunction with a near-wall k-ε model, and Koschel *et al.*[33] who used an unstructured finite-element scheme with no turbulence model. The success of these simulations in predicting mean quantities such as the pressure distribution around the sphere was limited. All calculations showed that the "steady" numerical solution is not axisymmetric, however, the presence of shedding was not investigated, as the simulations were not time-accurate. Finally, in a related study, Constantinescu and Squires[34] presented RANS calculations at $\mathrm{Re}=10^4$ using several models (k-ε, k-ω, S-A, $v2$-f). The level of accuracy in the prediction of the main time-averaged flow parameters differed from model to model with the two-layer k-ε showing the worse agreement with LES predictions and experimental measurements. Though time-accurate, the equilibrium RANS solution in these computations was practically steady-state in contrast to similar results obtained for RANS simulations of flow past cylinders. This might be attributed to the fact that the coherence of the wake structures in the flow past spheres is less significant as compared to the flow past cylinders.

IV. COMPUTATIONAL APPROACH

A. Detached-eddy simulation

DES is a nonzonal technique that can be applied at high Reynolds numbers as can RANS methods, but also resolves time-dependent, three-dimensional turbulent motions as in LES. The technique is based on a modification to the length scale in the destruction term of the one-equation eddy viscosity (S-A) model developed by Spalart and Allmaras.[35] Essentially, DES reduces to a RANS closure in the attached boundary layers (using the S-A model) and to a Smagorinsky-type subgrid scale model away from the wall.[1] There is a single solution field, and the transition between the RANS and LES regions, all coupled by the Navier–Stokes equations, is seamless in an application sense, i.e., without artificial transitions between the solution domains. Compared to URANS, for a fully three-dimensional flow DES is more expensive as typically the time steps are smaller and the grid in some regions of the flow has to be refined to capture the dynamically important eddies in that region (e.g., the vortex tubes in the detached shear layers that are not captured by URANS), but the overall increase is generally less than one order of magnitude. The difference is higher for flows that in average are two-dimensional.

In the S-A RANS model, a transport equation is used to compute a working variable, $\tilde{v}$, used to form the turbulent eddy viscosity, v_t. The DES formulation is obtained by replacing the distance to the nearest wall, d, by $\tilde{d}$ in the production/dissipation terms and model parameters. The distance $\tilde{d}$ is defined as

$$\tilde{d} \equiv \min(d, C_{\mathrm{DES}}\Delta), \quad \Delta \equiv \max(\Delta x, \Delta y, \Delta z), \tag{1}$$

where Δx, Δy, and Δz are the grid spacings. In "natural" applications of DES, the wall-parallel grid spacings (e.g., streamwise and spanwise) are at least on the order of the boundary layer thickness and the S-A RANS model is retained throughout the boundary layer, i.e., $\tilde{d}=d$. Consequently, prediction of boundary layer separation is determined in the "RANS mode" of DES. Away from solid boundaries, the closure is a one-equation model for the modified SGS eddy viscosity:

$$\frac{D\tilde{v}}{Dt} = c_{b1}[1-f_{t2}]\tilde{S}\tilde{v} - \left[c_{w1}f_w - \frac{c_{b2}}{\kappa^2}f_{t2}\right]\left[\frac{\tilde{v}}{\tilde{d}}\right]^2 + \frac{1}{\sigma}[\nabla\cdot((v+\tilde{v})\nabla\tilde{v}) + c_{b2}(\nabla\tilde{v})^2]. \tag{2}$$

The eddy viscosity v_t is obtained from

$$v_t = \tilde{v} f_{v1}, \quad f_{v1} = \frac{\chi^3}{\chi^3 + c_{v1}^3}, \quad \chi = \frac{\tilde{v}}{v}, \tag{3}$$

where v is the molecular viscosity. The production term is expressed as

$$\tilde{S} = S + \frac{\tilde{v}}{\kappa^2\tilde{d}^2} f_{v2}, \quad f_{v2} = 1 - \frac{\chi}{1+\chi f_{v1}}, \tag{4}$$

where S is the magnitude of the vorticity. The function f_w is given by

$$f_w = g\left[\frac{1+c_{w3}^6}{g^6+c_{w3}^6}\right]^{1/6}, \quad g = r + c_{w2}(r^6 - r), \quad r = \frac{\tilde{v}}{\tilde{S}\kappa^2\tilde{d}^2}. \tag{5}$$

The function f_{t2} is defined as

$$f_{t2} = c_{t3}\exp(-c_{t4}\chi^2). \tag{6}$$

The wall boundary condition is $\tilde{v}=0$ and the constants are $c_{b1}=0.1355$, $\sigma=2/3$, $c_{b2}=0.622$, $\kappa=0.41$, $c_{w1}=c_{b1}/\kappa^2+(1+c_{b2})/\sigma$, $c_{w2}=0.3$, $c_{w3}=2$, $c_{v1}=7.1$, $c_{t3}=1.1$, and $c_{t4}=2.0$. When the production and destruction terms of the model are balanced (the flow is near equilibrium), the length scale $\tilde{d}=C_{\mathrm{DES}}\Delta$ in the LES region yields a Smagorinsky eddy viscosity $\tilde{v}\propto S\Delta^2$, which varies in both space and time. The solution of the transport equation for the eddy viscosity accounts for transport and history effects analogous to dynamic formulations. The length scale redefinition away from solid boundaries increases the magnitude of the destruction term in the S-A model, drawing down the eddy viscosity and allowing instabilities to develop. Analogous to classical LES, the role of Δ is to allow the energy cascade down to the grid size; roughly, it makes the pseudo-Kolmogorov length scale, based on the eddy viscosity, proportional to the grid spacing. The additional model constant $C_{\mathrm{DES}}=0.65$ was calibrated in homogeneous turbulence.[36] Additional discussion of the model and implementation details can be found in Refs. 1, 3, and 4. The sensitivity of DES to the value of the model constant C_{DES} was investigated by Constantinescu and Squires[4] for the flow past spheres in the subcritical regime, also finding that a value $C_{\mathrm{DES}}=0.65$ was optimal.

Downloaded 19 Jul 2004 to 195.83.232.39. Redistribution subject to AIP license or copyright, see http://pof.aip.org/pof/copyright.jsp

B. Simulation overview

The incompressible flow around a sphere is computed using a fully implicit fractional-step method. The governing equations are transformed to generalized curvilinear coordinates with the primitive velocities and pressure retained as the dependent variables on a nonstaggered grid. Constantinescu and Patel[37] previously employed the base numerical method for computation of steady flows. The convective terms in the momentum and turbulence transport equations are discretized using a blend of fifth-order accurate upwind differences near the sphere walls and in the irrotational outer part of the flow and second-order central differences in the sphere wake region following ideas proposed by Travin *et al.*[38] and Strelets.[3] Similar to the cylinder calculations reported in these references, the switching insures that central differences are used over the wake region as well as over most of the detached shear layers. Upwind discretization is applied over the small upstream part of the detached shear layers, in the irrotational regions outside the wake and in the attached boundary layers on the back of the sphere. The source terms in the S-A model employed in DES are treated implicitly. All other operators in the momentum and pressure-Poisson equation are approximated using second-order central differences. Extension to time-accurate calculations was achieved using a double-time-stepping algorithm. The approximate factorization of the momentum and pressure-Poisson equations and the use of the local-time-stepping procedure are made in pseudo-time, and thus do not affect the time accuracy of the solution.

Solutions are obtained on a domain that extends from the sphere surface ($r=0.5$ D, where D is the sphere diameter) to 14.5 D in the radial direction. The governing equations are solved on simple O–O grid with (r,φ,θ) the radial, polar, and azimuthal directions, respectively. The grid is created by initially generating a two-dimensional mesh in an azimuthal plane r-φ and rotation around the polar axes. The grid points in the azimuthal direction are uniformly distributed. Most calculations were carried out on a baseline mesh of 141*101*41 points in the (r,φ,θ) directions as well as on a grid with refinement in the azimuth to 141*101*82 points. The first wall-normal grid point was within one viscous unit from the sphere surface ($\Delta r_1^+<1$, where $\Delta r^+=u_\tau \Delta r/\upsilon$ and $u_\tau=0.04$ U is used as a conservative estimate of the friction velocity). The distribution of the points near the sphere was dependent on the Reynolds number such that around 5–8 points were within ten wall units in the turbulent wake region for both the subcritical and supercritical calculations. For instance, at $\mathrm{Re}=10^4$ the maximum grid spacing near the sphere surface is roughly 9 wall units in the polar direction and 21 wall units in the azimuth (sensibly smaller in the turbulent wake because of the grid topology). This insures adequate resolution not only of the large-scale vortices in the wake but also of the vortex tubes in the detached shear layers. For the simulations of the supercritical flows a more substantial fraction of the turbulent motions are modeled, in turn providing a useful test of the predictive capability of DES at the higher Reynolds numbers considered.

The conditions at the upstream boundary ($r=14.5$ D, $0<\varphi<0.55\pi$) consist of a uniform velocity U. For solutions of the subcritical flows the inflow eddy viscosity was set to zero with nonzero values seeded into the wake. The reversing flow that is established in the wake region is sufficient to sustain the turbulence model downstream of separation in the subcritical solutions. Predictions of the supercritical flows with fully turbulent attached boundary layers were obtained by seeding a small level of eddy viscosity into the inflow condition, sufficient to ignite the turbulence model as the fluid enters the boundary layers on the sphere surface. As shown below, this treatment is simplistic and only a rough approximation to the boundary layer treatment on the sphere in the supercritical regime (quiet conditions and no tripping in experiments) for which part of the boundary layer is not turbulent. As also discussed in the following section, the differences in the DES predictions of the skin friction for the supercritical flows compared to the experimental measurements motivated simulations that attempted to more closely mimic boundary layer evolution prior to separation. Calculations were performed in which the turbulent eddy viscosity was suppressed prior to the azimuthal location at which transition is apparent in the measurements.

The velocity components and turbulence variables at the downstream boundary ($r=14.5$ D, $0.55\pi<\varphi<\pi$) are obtained using second-order extrapolation from the interior of the domain. The value of 0.55π corresponds to minimum distortions observed in the region in which the shed vortices cross the boundary. No-slip conditions on the sphere surface are imposed. The pressure boundary condition on the sphere, at the upstream and downstream boundaries is obtained from the surface-normal momentum equation. Periodic boundary conditions are imposed on all variables in the azimuthal direction. On the polar axes, $(\varphi=0,\pi)$, the dependent variables are obtained by averaging over the azimuth a second-order accurate extrapolation of these variables.

The convergence criterion at every time step was that the maximum value of the nondimensional velocity and pressure residuals should be smaller than 10^{-4} (D and U were used to nondimensionalize the residuals). This insured a reduction of more than two orders of magnitude for the norm of the velocity components to reach incompressibility at each physical time step, and yielded an adequate damping of errors throughout the entire domain. An average of about 60 subiterations were used to converge the solution per physical time step.

The temporal accuracy of the numerical approach was established[4] through comparison of the results from a simulation at $\mathrm{Re}=300$, in the (laminar) periodic vortex-shedding regime, with previous computational results and experimental measurements. For the same Reynolds number the size of the computational domain was increased up to 30 D in the radial direction. The resulting forces on the cylinder (mean value and amplitude of oscillation) and the shedding frequency were practically unaffected by the change in the domain size. For turbulent calculations, Constantinescu and Squires[4] previously compared DES to LES predictions obtained using a dynamic Smagorinsky model for the flow past a sphere at $\mathrm{Re}=10^4$, finding good agreement between the two techniques against experimental measurements. That in-

Downloaded 19 Jul 2004 to 195.83.232.39. Redistribution subject to AIP license or copyright, see http://pof.aip.org/pof/copyright.jsp

vestigation also showed the essential role played by the turbulence model, in that calculations attempted without any explicit model were numerically unstable, with the instability originating in the detached shear layers.

The present calculations were performed using a physical time step of 0.02 D/U, which insures that a period corresponding to the main shedding frequency corresponds to approximately 220 time steps in the subcritical regime and around 35 time steps in the supercritical regime. The influence of the time step was assessed in separate calculations in both the subcritical[4] and supercritical regimes to confirm that the unsteady features of the flow were adequately resolved. Halving the time step from the value used to obtain the results presented in the next section does not lead significant variations in the solutions.

V. RESULTS

Comparison between the predictions obtained at Re $=10^4$ and of the supercritical flow with fully turbulent boundary layers at Re$=1.14*10^6$ allows the assessment of the changes in the flow from the subcritical to supercritical regime. The influence of the boundary layer treatment for Reynolds numbers below the critical value is illustrated by comparing the solutions at the same Reynolds number, Re $=10^5$, with either a laminar or turbulent boundary layer separation, controlled in the computations via prescription of the upstream eddy viscosity. For higher Reynolds numbers (above the critical value $\mathrm{Re}_{\mathrm{cr}}$ in experiments) the effect of laminar-to-turbulent transition (as specified by the position at which the turbulence model becomes active) is investigated by comparing the fully turbulent solution at Re$=1.14*10^6$ to that obtained by suppressing the eddy viscosity to the location corresponding to transition observed in experiments at the same Reynolds number. The effect of Reynolds number in the supercritical regime for $\mathrm{Re}>\mathrm{Re}_{\mathrm{cr}}$, is considered by comparing the fully turbulent solutions at Re$=4.2*10^5$ and $1.14*10^6$.

A. Statistical features

Each simulation is integrated until a ''statistically quasi-stationary state'' develops. The transient to achieve this equilibrium required at least 30 D/U time units. The simulations are then integrated for an additional interval (30–60 D/U) that is used to acquire statistics of the flow. For the subcritical regime this corresponds to about 8–12 vortex-shedding cycles, while for supercritical Reynolds numbers this corresponds to about 40–80 oscillatory cycles of the dominant frequency.

Some of the global features of the simulations described below are summarized in Table I, where the mean streamwise drag coefficient, C_d, and its root mean square (r.m.s.) value, the ratio between the friction drag and the total drag, C_τ/C_d, the (polar) separation angle on the sphere measured from the stagnation point, φ_s (the interval denotes variations due to the shedding), and the polar angle corresponding to the end of transition, φ_t, are given along with the experimental measurements from Achenbach (1972). The location at which the turbulence model becomes active is estimated using the ''turbulence index.''[35] For DES it is evaluated using $i_t=(1/\kappa)u_\tau\partial\tilde{v}/\partial n$, where κ is the von Karman constant and n describes the coordinate normal to the wall. The index is zero in a laminar region, followed by a sharp increase in the predicted region of transition and in fully turbulent regions. In Table I the indices (s) and (S) indicate the nature of the attached boundary layer at separation (laminar or turbulent), while (ft) indicates that the boundary layer was turbulent from the stagnation point $(\varphi_t=0)$.

For the subcritical solution at Re$=10^4$, (laminar) boundary layer separation occurs at an angle of 85° that is slightly higher than the value of 82.5° measured by Achenbach.[5] Bakic[13] measured an angle of 80°–83° at a higher Reynolds number (Re$=5*10^4$) very close to the range obtained in the present subcritical solution at Re$=10^5$ (80.5°–82.5°). As discussed above, the calculations at Re$=10^5$ illustrate the important influence of boundary layer treatment (laminar or turbulent) that leads to different solutions due to the change in flow separation characteristics. As shown in detail in the following, the subcritical solution at Re$=10^5$ is very similar to that obtained at Re$=10^4$, while the supercritical solution at Re$=10^5$ resembles the supercritical solutions obtained at higher Reynolds numbers. As also summarized in Table I, in the supercritical simulations separation was predicted over an azimuthal angle range of $\varphi_s=114°-120°$ (depending on the Reynolds number and the location at which the turbulence model was active), these values being close to the measurements which indicate flow detachment around 119°–120°.

The prediction of the mean drag coefficient in the subcritical regime is within the range of the experimentally measured values for each of the Reynolds numbers considered. At Re$=10^4$ the predicted value is $C_d=0.393$ compared to $C_d=0.39-0.41$[5,9] in experiments while the DES prediction at at Re$=10^5$ is $C_d=0.414$ compared to $C_d=0.40-0.49$[5,9] for $10^5<\mathrm{Re}<\mathrm{Re}_{\mathrm{cr}}$, with increase in the measured C_d generally observed for higher Reynolds numbers approaching the drag crisis. The drag coefficient in the supercritical solution at Re$=10^5$ is sensibly lower compared to the one corresponding to the subcritical one (0.191 vs 0.414), a result of the change in the boundary layer separation characteristics. A similar trend was observed by Maxworthy[8] over this region (see Fig. 1) in which the boundary layer was tripped at $\varphi_t=55°$ in the experiment. The fully turbulent treatment in the computations yields a drag coefficient for the supercritical solution at Re$=10^5$ around $C_d=0.191$ which is lower than the drag measurements[8] $(C_d=0.27)$, consistent with the earlier transition to turbulence in the simulations.

As shown in Table I, for the supercritical cases the drag coefficient predicted in the DES is in good agreement with the experiments.[5,9] The agreement is especially satisfactory at Re$=4.2*10^5$ where the DES result of $C_d=0.093$ from a calculation in which transition was forced at $\varphi_t=100°$ (by suppressing the eddy viscosity) is close to the experimental value of 0.085.[9] Achenbach[15] measured several values for C_d at Re$=4.2*10^5$ between 0.07 and 0.09. The agreement is somewhat less satisfactory at Re$=1.14*10^6$ for both simulations.

Solutions obtained at Re$=10^5$ demonstrate the influence

Downloaded 19 Jul 2004 to 195.83.232.39. Redistribution subject to AIP license or copyright, see http://pof.aip.org/pof/copyright.jsp

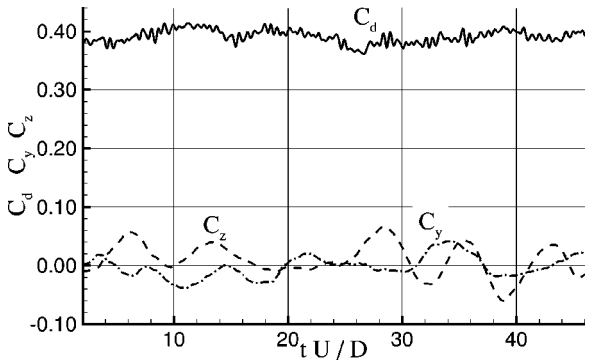

FIG. 2. Temporal evolution of the streamwise and lateral force coefficients, $Re=10^4$.

of the type of boundary layer separation on substantially altering the location of flow detachment, e.g., from 81.5° for the subcritical solution to 103° for the fully turbulent one. For the higher Reynolds numbers, suppressing the eddy viscosity in order to alter the location of transition results in a slightly delayed separation compared to the fully turbulent run (e.g., from 120° to 117° at $Re=1.14*10^6$). This also contributes to the higher drag for the fully turbulent runs as shown in Table I and Fig. 1.

The force histories in Figs. 2 and 3 provide a quantitative measure of the chaotic nature of the flow resulting from vortex shedding around the sphere in the subcritical ($Re=10^4$) and supercritical regime ($Re=1.14*10^6$, fully turbulent boundary layer). In addition to the streamwise (drag) force, the two lateral (side) force coefficients are shown. Somewhat apparent in Fig. 2 ($Re=10^4$) is a modulation in the drag coefficient, similar to that observed by Travin *et al.*[2] in the flow around a circular cylinder, though for the sphere the modulation is not as pronounced compared to the one for the cylinder (e.g., of the order of less than 5% for the sphere compared to about 20% for the cylinder). In fact, even larger modulations were obtained in a study of the flow around a flat plate[39] at 90°. Resolving accurately the low frequency end of the spectrum associated with this irregular modulation (especially in the subcritical regime) would require running the code for 300–500 time units. However, as for the sphere the amplitude of the modulation seems to be much smaller than in the case of cylinders and flat plates, and the statistics were calculated using samples containing around 10 shedding cycles, we think that the statistics are reasonably converged. In the results corresponding to the supercritical regime the temporal variation of the side-force coefficients displays a predominantly lower frequency than occurs in the variation of the drag coefficient, with in addition, larger deviations from the mean values.

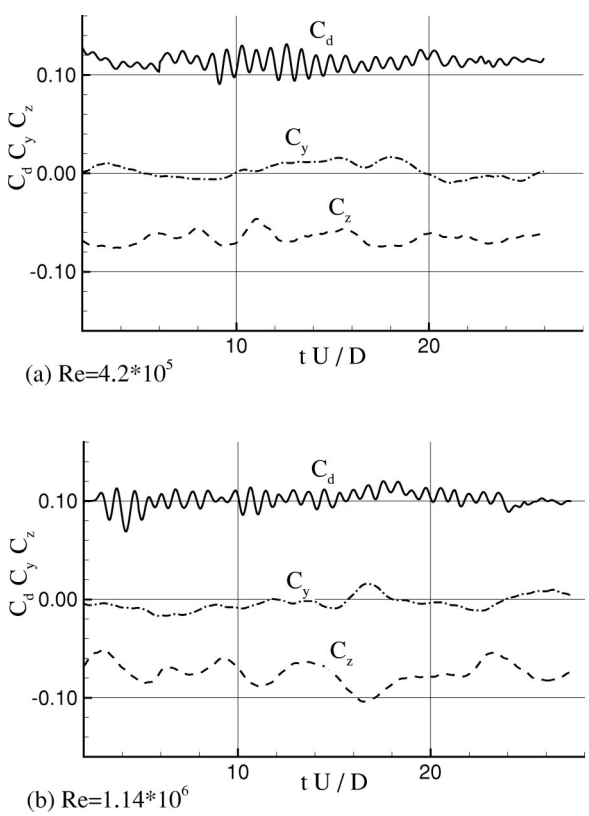

FIG. 3. Temporal evolution of the streamwise and lateral force coefficients (a) $Re=4.2*10^5$. (b) $Re=1.14*10^6$.

Frequency spectra of the drag coefficient for the subcritical flow at $Re=10^4$ and turbulent separation cases with $\varphi_t=0°$ and $\varphi_t=\varphi_t$ (experiment) at $Re=4.2*10^5$ and $Re=1.14*10^6$ are shown in Fig. 4. In the subcritical regime the main shedding frequency is predicted at a Strouhal number of 0.195, in agreement with the measured[12,15,28] range of St $\sim$0.19–0.2. In addition to the vortex shedding frequency, the spectrum also shows secondary peaks at St=1.9–2.4. This higher-frequency component is also visible in the time-history of C_d in Fig. 2, and is associated with the Kelvin–Helmholtz instability in the detached shear layers. The computed range of the shear-layer frequency is in close agreement with the range of 2.0–2.5, measured[12] at the same Reynolds number.

At Reynolds numbers higher than the critical one, there is a pronounced change in the general form of the temporal variation of the drag as can be observed in Fig. 3 at both Reynolds numbers, where only a single dominant frequency is present. Indeed, the frequency spectra in Fig. 4 show that for all simulations above Re_{cr} most of the energy of the drag fluctuations is concentrated around St=1.3–1.4 which is about seven times higher than the value associated with large-scale vortex shedding in the subcritical regime. Figures 4(b) and 4(c) also show that the spectra for the supercritical solutions lack the high frequency peak associated with rollup of the detached shear layers in the flow experiencing laminar separation. This may be a consequence that in the supercritical regime there is no other instability mode associated with a deterministic unsteadiness of the flow or, more likely, such frequencies are too high to be resolved by the present simulations. Flow visualizations of the turbulent separation cases described later do not show the formation of vortex tubes in the detached shear layers. And as also shown later, for flows with turbulent boundary layer separation the wake reorganizes into a configuration different from the subcritical solutions.

Related to the temporal variation of the lateral-force coefficients a number of interesting observations can be made.

Downloaded 19 Jul 2004 to 195.83.232.39. Redistribution subject to AIP license or copyright, see http://pof.aip.org/pof/copyright.jsp

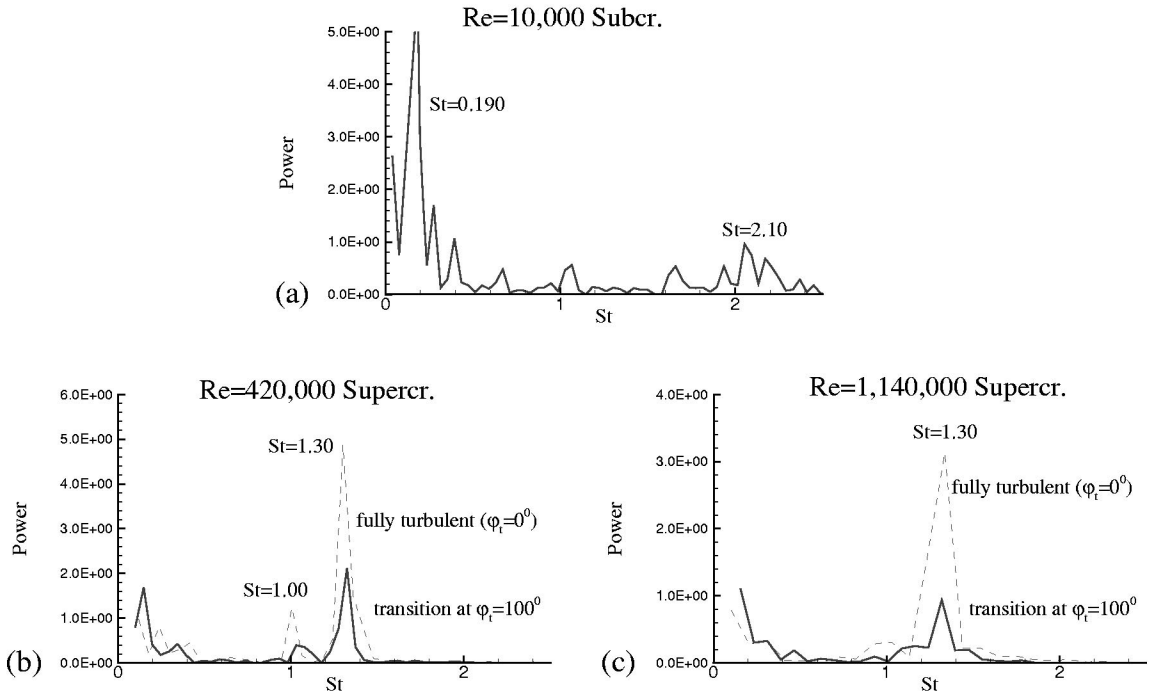

FIG. 4. Power spectra of the streamwise drag coefficient (a) Re$=10^4$. (b) Re$=4.2*10^5$. (c) Re$=1.14*10^6$.

Visualizations of the time history of the lateral force coefficients at Re$=10^4$ in two perpendicular planes (Fig. 2) reveal that the direction after which these vortices are shed, which roughly corresponds to the direction of the resultant side force on the sphere, oscillates with no regular pattern. The r.m.s. values of the components of the lateral-force are practically the same and over a sufficiently long interval the mean of both components are close to zero (within statistical uncertainty). Unlike the behavior observed in Fig. 2 for laminar separation, the side force on the sphere in the flow experiencing turbulent boundary layer separation is nonzero even in the mean (see Fig. 3 for both Re$=4.2*10^5$ and Re $=1.14*10^6$) suggesting that the wake may have some preferential orientations during the vortex shedding. This feature is analogous to the behavior observed in the nonaxisymmetric laminar shedding regime in low-Reynolds number sphere wakes ($280<$Re<350) in which the lateral force in the "shedding plane" exhibits a sinusoidal oscillation with a nonzero mean while in the plane perpendicular to the shedding plane the lateral force is zero for all times.[18] However, in the supercritical regime, due to the turbulence, the direction of the side-force seems to mutate about some equilibrium position. For example, in the fully turbulent calculation at Re$=1.14*10^6$ the mean of $C_y(\sim 0.005)$ is clearly different from the mean of C_z (~ -0.080) and C_z assumes negative values throughout the time history as shown in Fig. 3. The presence of a nonzero side force was observed in experimental investigations.[10] This would in turn indicate a possible lock-on phenomenon around an equilibrium position determined in the numerical simulations by the initial perturbed solution. However, as discussed by Travin *et al.*[2] in connection to the cylinder, it may be possible that there is an overall rotation of the wake occurring at a very low frequency which, if it were possible to acquire statistics over extremely long sampling times, would indicate that the average side force is zero. As discussed below, the nonzero side force is consistent with the flow visualizations in Figs. 10–12 that show the wake is dominated by the shedding of hairpin-like vortices at approximately the same orientation (azimuthal angle). An additional difference between the subcritical and supercritical regimes is that the r.m.s. of the side forces on the sphere are 4–10 times smaller than the drag force in the subcritical regime, though these forces are comparable in the supercritical regime.

The power spectrum of lateral forces at Re$=10^4$ [Fig. 5(a)] shows the presence of two dominant frequencies corresponding to St$=0.06$–0.08 and 0.15–0.16, which are lower than the one observed for the streamwise drag (St$=0.195$). However, there is no high-frequency component (around St $=2.0$) in the spectra of the lateral force coefficients that may be associated with the shear-layer instabilities. This is explained by the fact that the vortex tubes that are shed at the higher Strouhal number are positioned approximately in planes perpendicular to the freestream direction and the resulting force on the sphere is oriented parallel to this (streamwise) direction. The power spectra in Fig. 5(b) show that for supercritical flows (e.g., Re$=4.2*10^5$ and $1.14*10^6$) the main frequency associated with the lateral force oscillations is around St$=0.235$, which is about six times lower than the Strouhal number associated with the dominant frequency of the streamwise drag. The fact that the lateral force oscillates at significantly lower frequencies than the drag is not limited to the sphere, as for cylinders the lift oscillates at the shedding frequency while the drag oscillates at about two times that value.[2,25]

The distributions of the pressure coefficient C_p and skin

Downloaded 19 Jul 2004 to 195.83.232.39. Redistribution subject to AIP license or copyright, see http://pof.aip.org/pof/copyright.jsp

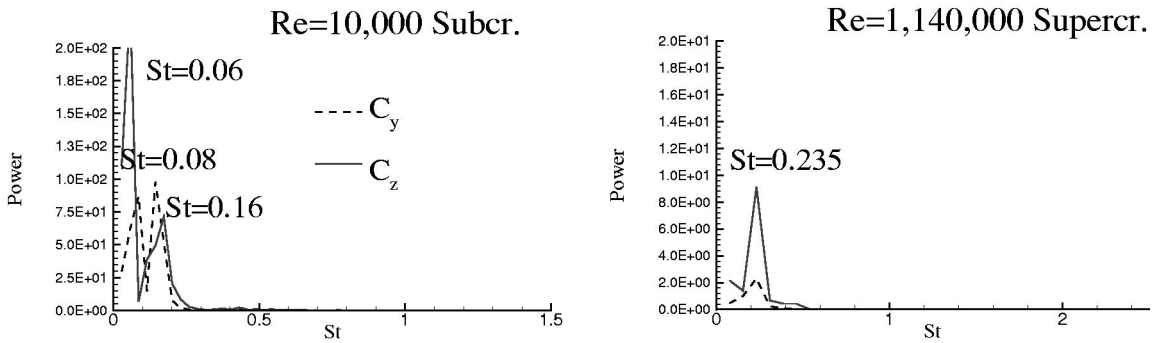

FIG. 5. Power spectra of the lateral force coefficient (a) Re$=10^4$. (b) Re$=1.14*10^6$ (fully turbulent).

friction coefficient C_τ (averaged over time and azimuthal direction) around the sphere are plotted in Figs. 6 and 7 for both subcritical and supercritical solutions. The skin-friction coefficient was nondimensionalized by $\rho U^2\sqrt{\mathrm{Re}}$ to allow a direct comparison between the changes in the distributions of C_τ over the sphere with the Reynolds number, and to be able to compare with available measurements at Reynolds numbers different than those considered in the simulations. In the subcritical regime the experimental data[5] at Re$=1.65*10^5$ (for quiet conditions) is used to evaluate the simulation at Re$=10^5$ and 10^4. As the figure shows, significant differences are observed in the pressure distribution, these differences mainly arising due to the state of the boundary layer prior to separation.

Predictions of C_p for the subcritical solutions at Re $=10^4$ and Re$=10^5$ are in good agreement with the measurements.[5] The value and angular position of the minimum in C_p are accurately captured, while the back pressure (at $\varphi=180°$) is slightly below the data. In the supercritical regime the delay in flow detachment substantially deepens C_p compared to the laminar separation solution. The supercritical predictions at Re$=10^5$ appear to be quite close to the measurements at Re$=3.18*10^5$ (around the value where the drag crisis occurs in quiet flows). Fully turbulent DES predictions at Re$=4.2*10^5$ and Re$=1.14*10^6$ are essentially the same. The value and angular position of the minimum in the pressure coefficient is also accurately predicted in the simulations compared to measurements. The experimental

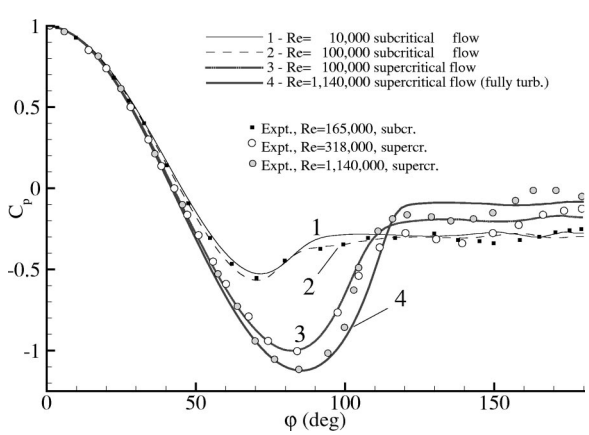

FIG. 6. Mean pressure coefficient.

distribution of C_p at Re$=1.14*10^6$ shows some variation in the pressure downstream of separation. In contrast, the DES predictions are relatively flat, above the data for polar angles between about 120 and 150° and then slightly below the data for $\varphi=150°$. The mismatch above and below the pressure measurements leads to a compensating effect such that the drag predictions are reasonably accurate. It is not clear why one gets this behavior of the pressure after separation, but one can speculate that the flow after separation is influenced by the transition region which is modeled with DES in RANS mode that, of course, cannot capture the details of transition. Though not shown in Fig. 6, the effect of forcing transition at the location observed in the experiment does not result in important modifications of the overall distribution of C_p, the only visible difference is a small decay of C_p at the end of the acceleration region and in the wake.

In the simulations of the subcritical flows the distribution of the skin-friction coefficient (Fig. 7) is in good agreement with the measurements[5] up to separation, while some disagreement exists in the turbulent wake region between predictions and experiment. The contribution of the friction forces to the total drag at Re$=10^4$ is approximately 8.5%. An extrapolation of the experimental data[5] measured at higher Reynolds numbers would indicate a value around 5.5% at Re$=10^4$. The agreement for this quantity is also very good for the subcritical calculation at Re$=10^5$ (2.2% vs 1.8% in experiment). Figure 7 shows that the fully turbulent treatment of the boundary layers at the higher Reynolds numbers leads to relatively large differences between the simulation results and experimental measurements. As described by Achenbach,[5] the process of boundary layer transition occurring in the experiments is complex, Fig. 7 indicating, for example, that substantial regions of the sphere boundary layers are laminar with a transition to turbulence in the vicinity of 90° prior to flow separation further aft. The DES prediction of the fully turbulent flow at Re$=1.14*10^6$, for example, yields a skin friction distribution far above the measured values with the ratio of C_τ/C_d approximately 15% and sensibly higher than the measured value of 7.5%.

Also shown in Fig. 7 are skin friction distributions obtained from computations in which the eddy viscosity was suppressed up to the position of transition observed in the experimental measurements. Though a crude approach to

Downloaded 19 Jul 2004 to 195.83.232.39. Redistribution subject to AIP license or copyright, see http://pof.aip.org/pof/copyright.jsp

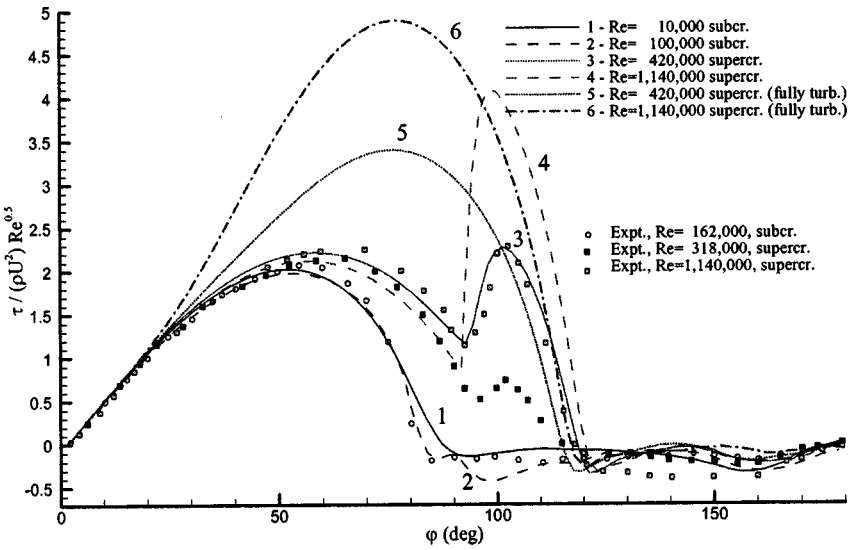

FIG. 7. Mean skin-friction coefficient.

"controlling" transition, the agreement with the experimental data is clearly improved, especially for $\mathrm{Re}=4.2*10^5$. The prediction captures accurately the relative minimum at the start of transition ($C_\tau=0.9$, experiments show $C_\tau=1.1$) as well as the relative maximum ($C_\tau=2.2$ in both simulation and experiment) and location ($\varphi=101°$) where the attached boundary layer becomes fully turbulent. Following separation, some disagreement is noted in the prediction of C_τ. As the Reynolds number is increased to $1.14*10^6$, the overall distribution of the skin-friction coefficient is similar, though the simulation substantially overpredicts C_τ in the region between the start of transition and separation. After separation, the accuracy of the predictions at the two Reynolds numbers is similar. The predictions of C_τ/C_d at $\mathrm{Re}=1.14*10^6$ are not as accurate in that the predicted ratio is 12%, while the measured value is 7.5%, but still somewhat better than the value predicted in the fully turbulent simulation (15.2%). In contrast, at $\mathrm{Re}=4.2*10^5$, the agreement with the experimental value is very good at around 13% as shown in Table I. Overall, the disagreement in the prediction of C_τ relative to the experimental data should not surprise, as RANS type models such as the S-A model cannot capture accurately the transition in the attached boundary layers.

B. Flow visualizations

In describing the differences between the subcritical and supercritical solutions it is helpful to delineate three main regions (recirculation, recovery, near-wake) in the wake. At $\mathrm{Re}=10^4$ the recirculation region extends between $x/D=0.5$ and 2.2, while the recovery region covers the range between $x/D=2.2$ and 4.5. The recovery region is defined as the area between the end of the recirculation region and the point on the polar axis where the flow accelerates despite the adverse pressure gradient. The shrinkage of the recirculation region in the supercritical flow was documented in experiments.[10] For instance, the length of the recirculation region decreases from 1.7 D at $\mathrm{Re}=10^4$ to about 0.6 D at $\mathrm{Re}=1.14*10^6$ (fully turbulent solution). The same is true for the recovery region, for instance at $\mathrm{Re}=1.14*10^6$ it extends between 1.1 and 2.4 D.

Shown in Fig. 8 are contours of the instantaneous vorticity magnitude in the sphere wake for the cases with laminar boundary layer separation at $\mathrm{Re}=10^4$ and with turbulent separation at $\mathrm{Re}=10^5$ and $\mathrm{Re}=1.14*10^6$ (delayed "transition" to $\varphi=\varphi_{\mathrm{exp.}}$ and fully turbulent cases). In the subcritical regime the vorticity contained in the large-scale shed vortices

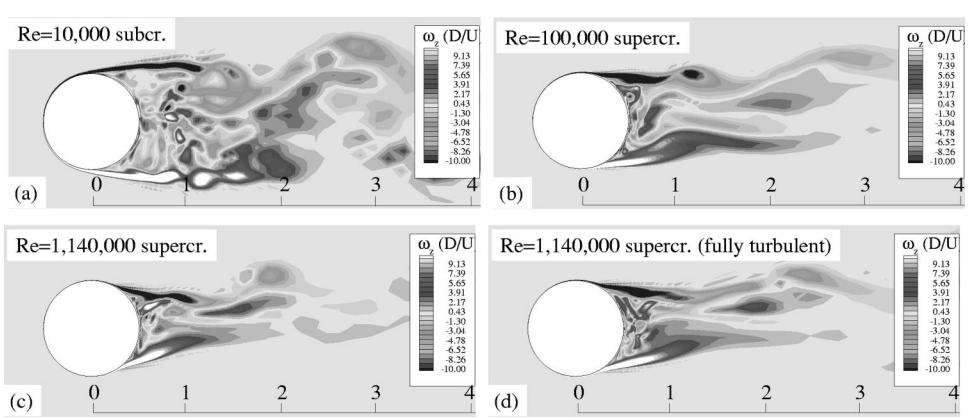

FIG. 8. Contours of the instantaneous out-of-plane vorticity component in an azimuthal plane (a) $\mathrm{Re}=10^4$. (b) $\mathrm{Re}=10^5$ (supercritical). (c) $\mathrm{Re}=1.14*10^6$. (d) $\mathrm{Re}=1.14*10^6$ (fully turbulent).

Downloaded 19 Jul 2004 to 195.83.232.39. Redistribution subject to AIP license or copyright, see http://pof.aip.org/pof/copyright.jsp

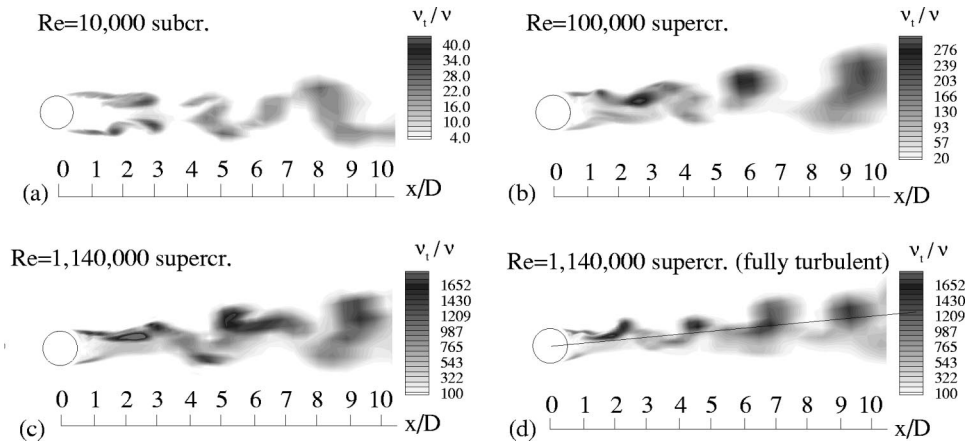

FIG. 9. Contours of the instantaneous eddy viscosity in an azimuthal plane (a) $\mathrm{Re}=10^4$. (b) $\mathrm{Re}=10^5$ (supercritical). (c) $\mathrm{Re}=1.14*10^6$. (d) $\mathrm{Re}=1.14*10^6$ (fully turbulent).

is originating mainly from the separated shear layers where the vortex tubes are forming. The Kelvin–Helmholtz rollup of the separated shear layers just downstream of flow detachment is resolved in the simulation at $\mathrm{Re}=10^4$ and the vortex tubes in the detached shear layers are visualized as successive patches of elevated out-of-plane vorticity in the detached shear layers [Fig. 8(a)]. The overall structure of the detached shear layers is similar to the one revealed by smoke and dye visualizations in experiments.[10,13] The average size of the vortex tubes increases with the distance from the separation point. Pairing of the vortex tubes into larger structures in the detached shear layers can be observed in experiments and in the current simulations (not shown) via examination of the temporal evolution of the patches of positive and negative vorticity associated with these vortices.

More information into the shedding mechanism (especially in the near-wake region where the "quasi-axisymmetric" character of the solution is lost) is provided by contours of the viscosity ratio v_t/v in Fig. 9 and by visualization of the vortical structures in the wake in Fig. 10 using the method of Jeong and Hussain[40] which targets swirling motions around local pressure minima. For the supercritical simulations the azimuthal plane chosen to show the eddy viscosity contours corresponds to the plane oriented in the direction of the lateral force. Though the unsteady flow over all Reynolds numbers considered here seems to be driven by the periodic growth of the wake and the release of hairpin-like vortices, there are obvious differences in the characteristic length- and time scales associated with the shedding of these vortices that are evident in Figs. 9 and 10 as one moves from subcritical to supercritical conditions. The distribution of the viscosity ratio demonstrates the ability of DES to predict zones of very low eddy viscosity in the region immediately behind the sphere where the grid density is high and a relatively large percentage of the total stress is resolved. Vorticity is fed into the wake through the detached shear layers in both regimes, as in these regions the turbulence SGS production is very high [see also Fig. 14(b)]. The relatively high values of the SGS viscosity observed in the large-scale structures convected downstream prove the increased influence of the turbulence model on the solution in the near-wake, where the grid is coarsening.

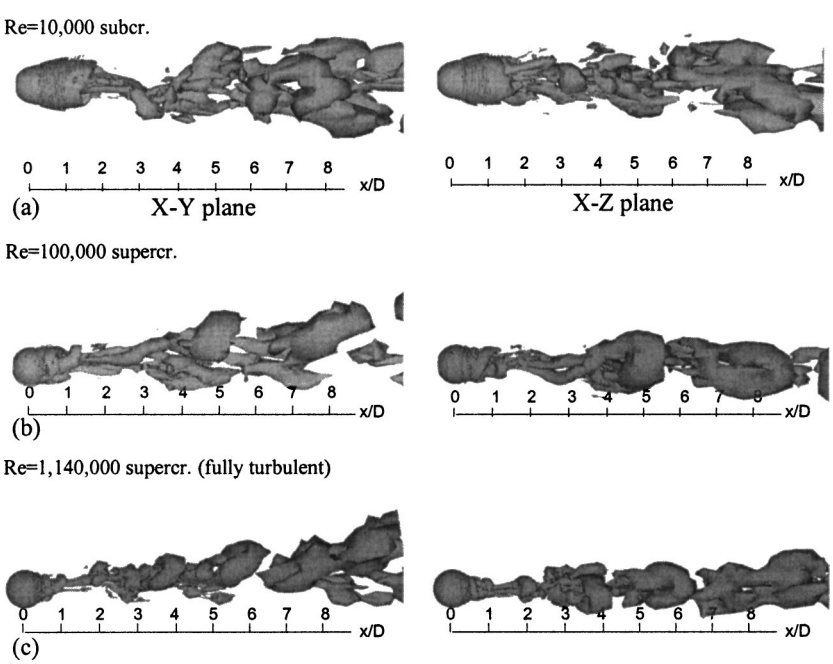

FIG. 10. Visualization of vortical structures using the method of Jeong and Hussain (1995) (a) $\mathrm{Re}=10^4$. (b) $\mathrm{Re}=10^5$ (supercritical). (c) $\mathrm{Re}=1.14*10^6$ (fully turbulent).

Downloaded 19 Jul 2004 to 195.83.232.39. Redistribution subject to AIP license or copyright, see http://pof.aip.org/pof/copyright.jsp

In the subcritical simulation in Fig. 10(a) the hairpin-like vortical structures become apparent some distance from the sphere, as near the sphere a compact vortical structure of a fairly axisymmetric shape that corresponds to the presence of vortex tubes in the detached shear layers is observed. Examination of the evolution in time of these structures shows that the azimuthal angles at which the vortices are formed and shed varies strongly in time, with the effect of creating a helical-like wake structure similar to what was observed in experiments. Some patches of vorticity are separating from these organized structures as they are convected downstream. The helical-like wake shape is also evident in Fig. 10(a). The overall form of the interconnected hairpin-like structures resembles one corresponding to a progressive wave motion of the wake.

Figures 9(d) and 10(c) corresponding to the fully turbulent simulation at $\mathrm{Re}=1.14*10^6$ show clear evidence of the presence of large-scale vortex shedding in the supercritical regime. The wake structure becomes more organized and more compact (something that was also observed in experimental visualizations of the supercritical wake), the large-scale eddies are shed at a more rapid rate compared to the simulation at $\mathrm{Re}=10^4$ (recall that the dominant frequency in the supercritical regime is much higher than the one associated with large-scale shedding in the subcritical regime). The orientation of the shedding is less variable, as the wake appears to undergo mutations around some equilibrium direction. The shedding appears to be locked around a certain azimuthal direction, at least for long intervals of time. The asymmetry is largest in the plane corresponding to the maximum instantaneous lateral force (plots shown on the left in Fig. 10). In visualization experiments at supercritical conditions, the shedding is not as easy to capture as for subcritical conditions because the spiraling mode is absent. This may explain why Taneda[10] did not observe vortex shedding in flow visualizations at $\mathrm{Re}>\mathrm{Re}_{\mathrm{cr}}$. The present results clearly indicate that large-scale coherent eddies are shed periodically and rather regularly into the wake, but in view of the above discussion the shedding process is of a different nature than the one observed for subcritical conditions. We suspect that by refining the mesh in the detached shear layers and the wake one will increase the range of resolved scales in the flow, and the large highly organized vortical structures seen in Fig. 10(c) will be somewhat affected, but we are reasonable confident based also on some mesh refinement studies not reported here that these structures will maintain their relative highly organized structure and they will continue to be the dominant coherent structures in the supercritical wake. The turbulence spectra may become richer especially at higher frequencies and very well resolved simulations may detect the shedding of small structures in the detached shear layers.

A consequence of the fact that the vortices are shed at about the same azimuthal angle is an overall asymmetry for the wake in the plane in which shedding takes place, an effect observed in flow visualizations.[10] The wake appears to tilt relative to the mean-flow direction in that azimuthal plane, while in the plane perpendicular to it, the shape remains fairly symmetric (plots shown on the right in Fig. 10).

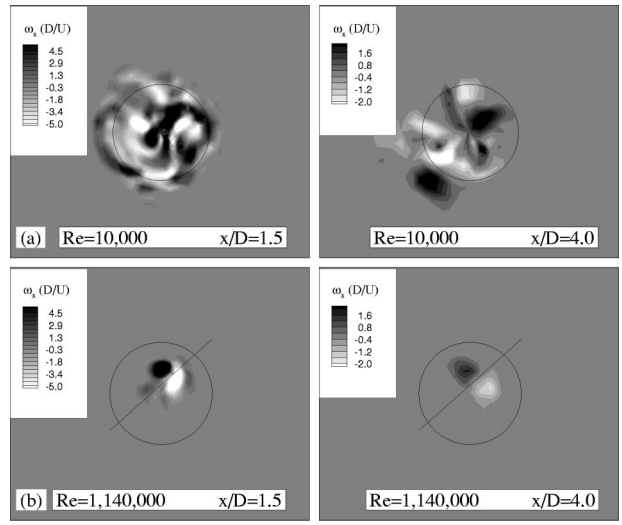

FIG. 11. Streamwise vorticity component in the crossflow plane at $x/D=1.5$ and $x/D=4.0$ (a) $\mathrm{Re}=10^4$. (b) $\mathrm{Re}=1.14*10^6$ (fully turbulent).

Another interesting feature visible in Fig. 10(c) is the formation of a horseshoe vortical structure behind the sphere, which one can speculate is similar to that described by Taneda[10] based on surface flow (oil) visualizations. The direction of the resulting lateral force on the sphere is along the approximate plane of symmetry of the horseshoe structure and of the hairpin-like structures shed in the wake. Also apparent in Fig. 9 is an increase in the coherence and organization of the vortical structures in the wake as the Reynolds number is increased in the supercritical regime, also consistent with a greater fraction of the turbulent motions being modeled at higher Reynolds number. Meanwhile, the effect of changing the position of transition on the sphere is negligible. The configuration of the near wake is similar in all supercritical cases.

Further details on the differences between the wake structures in the two regimes can be illustrated by examina-

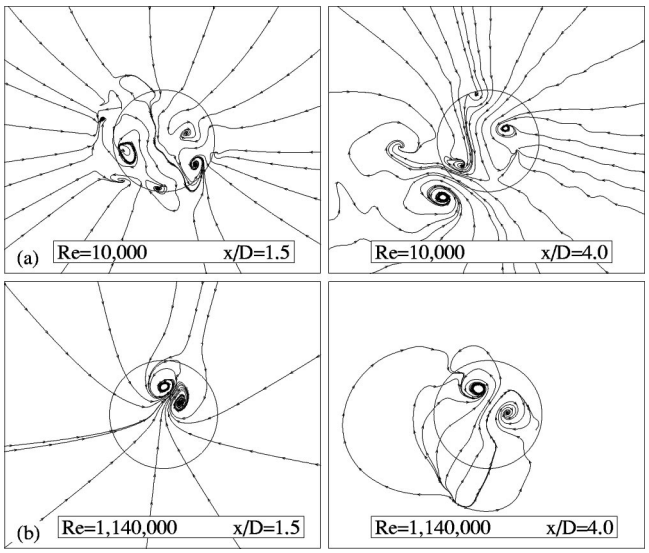

FIG. 12. Pathlines of the instantaneous flow in the crossflow plane at $x/D=1.5$ and $x/D=4.0$ (a) $\mathrm{Re}=10^4$. (b) $\mathrm{Re}=1.14*10^6$ (fully turbulent).

Downloaded 19 Jul 2004 to 195.83.232.39. Redistribution subject to AIP license or copyright, see http://pof.aip.org/pof/copyright.jsp

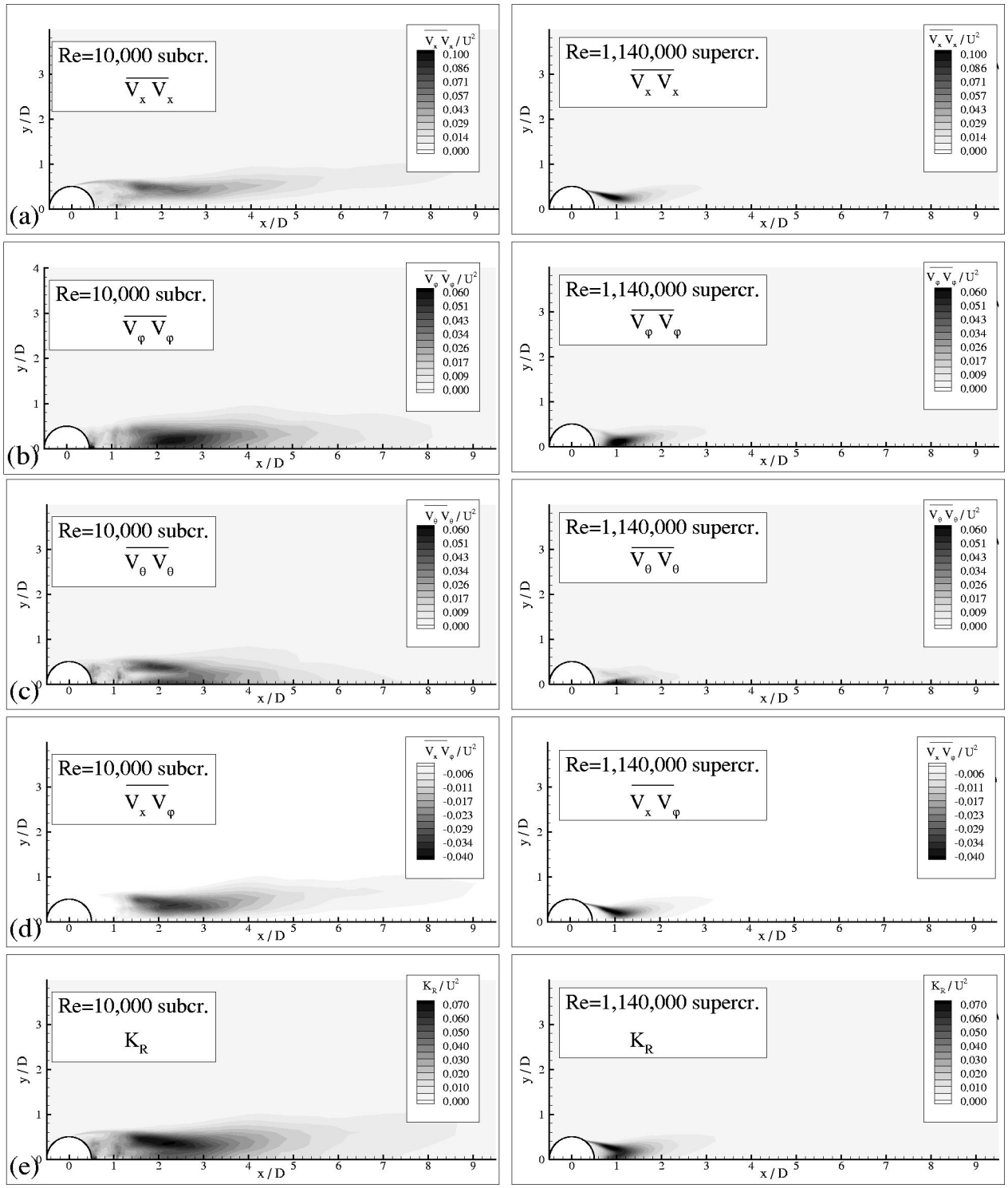

FIG. 13. Contours of the averaged resolved Reynolds stresses and kinetic energy in an azimuthal plane (a) $\overline{V_xV_x}$. (b) $\overline{V_\varphi V_\varphi}$. (c) $\overline{V_\theta V_\theta}$. (d) $\overline{V_xV_\varphi}$. (e) K_R.

tion of the distribution of the streamwise vorticity component (Fig. 11), and pathlines of the instantaneous solution (Fig. 12) in planes normal to the freestream direction, shown at 1.5 and 4.0 D from the center of the sphere in the figure. There is a striking difference in the wake structure in the solution at $\mathrm{Re}=10^4$ and the fully turbulent solution at $\mathrm{Re}=1.14*10^6$. Two concentrated patches of oppositely signed vorticity are evident in the supercritical solution at $x/D=1.5$, compared to the more chaotic and random pattern in the subcritical solution at the same downstream location. Further downstream ($x/D=4.0$), though the vortex patches are more diffused, the counter-rotating vortex pair corresponding to the cut through the legs of an earlier-shed hairpin vortex remains a clear feature of the flow in that section. By comparison, the subcritical simulations do not exhibit coherent structures of similar organization in the near wake. Comparing the two views of the instantaneous streamlines for the supercritical solution, the figure shows that the wake

Downloaded 19 Jul 2004 to 195.83.232.39. Redistribution subject to AIP license or copyright, see http://pof.aip.org/pof/copyright.jsp

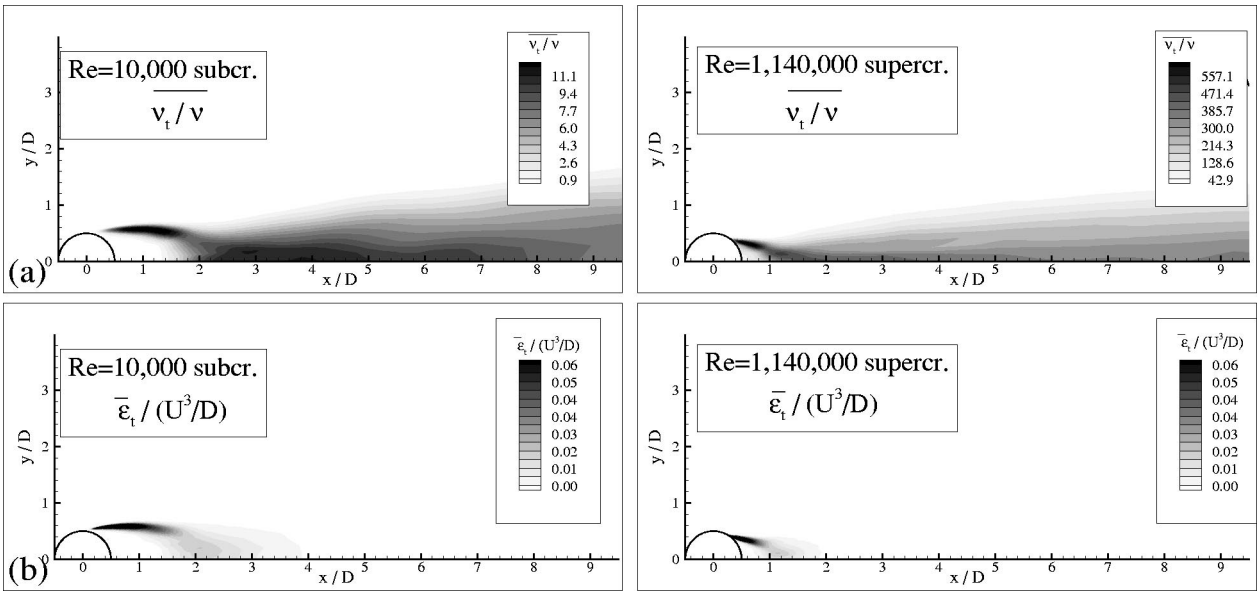

FIG. 14. Contours of the averaged subgrid scale viscosity and subgrid scale dissipation in an azimuthal plane (a) υ_t/υ. (b) ε_t.

has the same orientation (given by the plane perpendicular to the direction containing the legs of these hairpin vortices) at $x/D=1.5$ and 4, an effect that leads, as was already pointed out, to a mean nonzero side force. As expected, the dimension of the wake region in the subcritical case is sensibly larger compared to the supercritical case. For the supercritical simulation, the organization of the vorticity near the sphere into a horseshoe-like structure is suggested by the distribution of the instantaneous pathlines [Fig. 12(b)] in the section at $x/D=1.5$ (recall the sphere surface is at $x/D=0.5$) where the figure shows a vortex sheet whose ends roll up into two counter-rotating vortices.

As also discussed above, Taneda[10] proposed a more simple mechanism for the wake structure in the supercritical regime, that wake formation consisted of the shedding of a vortex sheet, whose ends began to roll up and form a pair of streamwise counter-rotating vortices in the wake. One should point out that the model proposed based on experimental visualizations[10] is based on theoretical reasoning and that it was not possible to clearly visualize the presence of those counter-rotating vortices. The action of these wake vortices on the sphere translates into a nonzero mean lateral force. The present simulations point to a somewhat different mechanism, in which the role of the two counter-rotating vortices is replaced by an array of hairpin-like vortices which are shed at a relatively high frequency and at about the same azimuthal angle over relatively long intervals of time. The mechanism of producing the lateral force is essentially the same, but the resultant lateral force is due to adding the contributions of the successively shed hairpin vortices. The proposed mechanism has the advantage that is consistent with the wake features observed in visualizations,[10] but also with the ones present in the current simulations. It may be likely that the failure to capture the presence of vortex shedding was based only on examination of the general form of the wake. The spiral instability, which translates into a wake that undergoes a progressive wave motion that was observed in experiments and in the present simulations with laminar separation, is absent in the cases with turbulent separation. Consequently, the overall shape of the wake may not appear to change significantly in time in experimental visualizations.

C. Subcritical vs supercritical turbulence statistics

The present simulations may be used to further investigate the differences in the flow structure, particularly in the detached shear layers and wake regions, between the subcritical and supercritical regime by comparing the distribution of the Reynolds stresses and other turbulent quantities between a simulation with laminar separation ($\mathrm{Re}=10^4$) and a simulation with turbulent separation (fully turbulent attached boundary layers at $\mathrm{Re}=1.14*10^6$). This is important because detailed experimental measurements over these regions are not available, particularly in the supercritical regime. Contour plots representing the statistics of the mean resolved turbulent fluctuations, the primary shear stress and resolved turbulent kinetic energy in an azimuthal plane are shown in Fig. 13, while the SGS viscosity and the SGS dissipation ε_t are shown in Fig. 14.

The distributions of the resolved part of turbulent fluctuations and resolved shear stress show that the spatial extent of the regions of high turbulent stress is much larger (up to three times) in the cases with laminar separation, especially in the streamwise direction. The areas of elevated turbulent stresses and turbulence kinetic energy are located within the recirculation and recovery regions for both laminar and turbulent separation, though the spatial distribution of these areas is different for the different components of the stress tensor. For example, high values of the streamwise fluctuations $\overline{V_xV_x}$ and primary shear stress $\overline{V_xV_\varphi}$ are observed in a region in the aft of the sphere located at about 0.3–0.4 D from the polar axis aligned with the freestream direction, while the fluctuations in the other two directions do not ex-

Downloaded 19 Jul 2004 to 195.83.232.39. Redistribution subject to AIP license or copyright, see http://pof.aip.org/pof/copyright.jsp

hibit elevated levels in this region. The streamwise length of this region for $\overline{V_x V_\varphi}$ [Fig. 13(d)] extends between 1.2 and 4.5 D in the laminar separation case and between 0.7 and 2.2 D in the turbulent separation case. The upper value corresponds approximately to the end of the recovery region in both cases. In the supercritical flow, high values of the shear stress are recorded over the whole separated shear layers, as opposed to the case with laminar separation where, as expected, the values are relatively low over the upstream part of the shear layers. Analysis of the other supercritical simulations showed that for $\mathrm{Re}>4*10^5$ the differences between the distributions of the primary shear stress in the wake disappear almost entirely regardless the location at which the turbulence model is activated.

It is also interesting to note that the shape of the regions of high values of a certain component of the Reynolds stress tensor are not very different in the subcritical and supercritical simulations, if one takes into account the general shrinkage of the recirculation and recovery regions in the simulation with turbulent separation. The nondimensional components of the Reynolds stress tensor display comparable ranges at both Reynolds numbers. Overall, negligible levels of the stress tensor are observed within the laminar regions and close to the sphere surface, indicating that DES responds correctly to the local-strain rates.

Regions of elevated eddy viscosity are predicted in both simulations [see Fig. 14(a)] over the downstream part of the detached shear layers as well as near the freestream-oriented polar axis at $x/D\sim 3.0$ in the simulation at $\mathrm{Re}=10^4$ and at $x/D\sim 1.5$ in the simulation at $\mathrm{Re}=1.14*10^6$. This is followed by a mild decay with the distance from the sphere of the SGS viscosity in the wake at both Reynolds numbers. Figure 14(b) shows the distribution of the turbulence energy dissipation, ε_t. The variation of the SGS dissipation in the wake is characterized mainly by a sharp increase in the detached shear layers. The elevated level of the SGS viscosity and strain rates in the shear layers are responsible for the (absolute) high levels of the SGS dissipation and the relative increase of the modeled part relative to the total shear stress observed in these regions.

VI. SUMMARY

The flow past a sphere is known to undergo significant changes when transition from subcritical to supercritical flow takes place or the flow is artificially tripped at Reynolds numbers below the critical value in experiments. In addition to the abrupt reduction in the drag, the sphere wake reorganizes due to the enhanced mixing of the flow. In this paper, predictions of the subcritical and supercritical flow over a sphere were obtained using detached eddy simulation. The DES predictions were able to resolve the organized motion in the near wake of the sphere and to capture many of the features that characterize the subcritical and supercritical regimes, as revealed by experimental investigations.

In the subcritical regime with laminar boundary layer separation DES was able to capture the large-scale shedding associated with the spiral instability of the wake, as well as the formation of the vortex tubes in the separated shear layers due to the growth of Kelvin–Helmholtz instabilities in these layers (e.g., see the visualizations of Taneda[10]). The agreement between DES and experimental data[5] was satisfactory in terms of global and local wake characteristics such as streamwise drag, location of transition on the sphere, and the distributions of the pressure and skin-friction coefficients. In the supercritical regime, DES accurately predicted the position of boundary layer separation and the distribution of the mean pressure coefficient over the sphere surface. In the fully turbulent cases the skin friction coefficient was not predicted accurately compared to the experiment. Improved agreement was obtained when the model was activated near the region where transition was observed in measurements. Though delaying activation of the model cannot represent the details of transition in the sphere boundary layers, this resulted in a clearly improved agreement for the prediction of the skin-friction coefficient. The main shedding frequency in the wake appears to be insensitive to the location at which the model was activated in the supercritical regime and, to a certain extent, even to the Reynolds number. Time histories of the forces and frequency spectra of the drag show that the supercritical solutions are chaotic and unsteady.

Both simulations and experimental measurements show that the subcritical regime is characterized by the presence of two main frequencies in the wake, one associated with the shedding at a Strouhal number $\mathrm{St}=0.19-0.20$ and one with the formation of the vortex tubes via the Kelvin–Helmholtz instabilities in the detached shear layers at a much higher Strouhal number (e.g., $\mathrm{St}\sim 2$ for $\mathrm{Re}=10^4$). In addition, the shedding of the large-scale vortex structures takes place at different azimuthal angles, with the effect of a helical-like form for the wake and the presence of a lateral force that averages to zero over relatively short time intervals. In contrast, simulations in which the attached boundary layer is turbulent at separation show that in this regime the wake is characterized by the presence of a dominant frequency at $\mathrm{St}=1.3-1.4$. The orientation of the shedding appears to be approximately locked on for time intervals that are of the order of 30–60 D/U which indicates a qualitative change in the shedding mechanism. However, it is possible that over larger time scales the orientation of the shedding will ''sample'' all azimuthal directions. The simulations accurately captured the downstream change in the separation location from 81° to 84° in the subcritical regime to 114°–120° in the supercritical regime. The simulations also represented the relative shrinking of the wake with Reynolds number and other features observed in experiments such as the increased compactness and coherence, and the general tilting of the wake. Based on these findings a new model describing the organization of the wake in the supercritical regime was proposed. This model is consistent with the wake features observed in previous experimental visualizations, but the wake structure is determined by shedding of hairpin-like vortices in a rather regular fashion at approximately the same azimuthal angle from the sphere over substantial time intervals. These structures do not rotate significantly as they are convected downstream. The two parallel legs of these hairpin-like structures rotate in opposite directions and induce a force in the direction perpendicular to the plane in

Downloaded 19 Jul 2004 to 195.83.232.39. Redistribution subject to AIP license or copyright, see http://pof.aip.org/pof/copyright.jsp

which these two legs are aligned. Successive hairpin vortices have contributions of unequal intensities to the resulting force on the sphere. The resultant contribution has the effect of tilting the wake, as observed in experiments, and consequently of inducing a nonzero side force.

Finally, DES of the subcritical flows does not fully test the method, i.e., the predictions are essentially a large eddy simulation (though the requirement the model remain dormant in the laminar regions of the flow is not trivial). Prediction of the supercritical flows experiencing turbulent boundary layer separation comprises a more stringent test because of the additional empiricism inherent in the boundary layer treatment. For the fully turbulent approach used in this work, the prediction of boundary layer separation is under the control of the RANS model. Inaccuracies in the prediction of boundary layer growth and separation will in turn have a more pronounced effect on the overall solution quality. In contrast, LES with wall-layer models[6,7] would necessarily resolve a fraction of boundary layer eddies. These approaches would in turn be expected to be less sensitive to modeling errors, though at considerable increase in computational cost at high Reynolds numbers. For DES, the present calculations of the supercritical flow yielded pressure distributions and values of the drag coefficient in good agreement with measurements and are useful in building confidence in the method, as well as understanding its limitations. As already discussed in reference to the skin friction distributions, the fully turbulent treatment is simplistic with the resulting skin friction above the measured distributions of the high Reynolds number experiments. Separated flows in which transition to turbulence and separation are inter-mingled will continue to pose strong challenges to all predictive strategies. This will continue to highlight the importance of boundary layer treatment of separating flows for applications at high Reynolds numbers.

ACKNOWLEDGMENTS

This work is supported by the U.S. Office of Naval Research (Grant Nos. N00014-96-1-1251, N00014-97-1-0238, and N00014-99-1-0922, Program Officers: Dr. Patrick Purtell and Dr. Candace Wark). The authors gratefully acknowledge valuable discussions with Dr. Philippe R. Spalart.

[1] P. R. Spalart, ''Strategies for turbulence modeling and simulations,'' Int. J. Heat Fluid Flow **21**, 252 (2000).
[2] A. Travin, M. Shur, M. Strelets, and P. R. Spalart, ''Detached-eddy simulations past a circular cylinder,'' Flow, Turbul. Combust. **63**, 293 (2000).
[3] M. Strelets, ''Detached eddy simulation of massively separated flows,'' AIAA Pap. 2001-0879 (2001).
[4] G. S. Constantinescu and K. D. Squires, ''LES and DES investigations of turbulent flow over a sphere at Re=10 000,'' J. Flow, Turbul. Combust. **70**, 267 (2003).
[5] E. Achenbach, ''Experiments on the flow past spheres at very high Reynolds numbers,'' J. Fluid Mech. **54**, 565 (1972).
[6] U. Piomelli and E. Balaras, ''Wall layer models for large eddy simulations,'' Annu. Rev. Fluid Mech. **34**, 349 (2002).
[7] M. Wang and P. Moin, ''Dynamic wall modeling for large eddy simulation of complex turbulent flows,'' Phys. Fluids **14**, 2043 (2002).
[8] T. Maxworthy, ''Experiments on the flow around a sphere at high Reynolds numbers,'' J. Appl. Mech. Trans. ASME, E **36**, 598 (1969).
[9] H. Schlichting, *Boundary-Layer Theory*, 7th ed. (McGraw-Hill, New York, 1979).
[10] S. Taneda, ''Visual observations of the flow past a sphere at Reynolds numbers between 10^4 and 10^6,'' J. Fluid Mech. **85**, 187 (1978).
[11] H. J. Kim and P. A. Durbin, ''Observations of the frequencies in a sphere wake and of drag increase by acoustic excitation,'' Phys. Fluids **31**, 3260 (1988).
[12] H. Sakamoto and H. Haniu, ''A study of vortex shedding from spheres in a uniform flow,'' J. Fluids Eng. **112**, 386 (1990).
[13] V. Bakic, ''Experimental investigation of turbulent flows around a sphere,'' Ph.D. thesis, TUHH Hamburg, Germany (2002).
[14] J. M. Chomaz, P. Bonneton, and E. J. Hopfinger, ''The structure of the near wake of a sphere moving horizontally in a stratified fluid,'' J. Fluid Mech. **254**, 1 (1993).
[15] E. Achenbach, ''Vortex shedding from spheres,'' J. Fluid Mech. **62**, 209 (1974).
[16] M. Provansal, ''From the double vortex street behind a cylinder to the wake of a sphere,'' Proceedings of the Conference on Bluff Body Wakes and Vortex-Induced Vibration (BBVIV3), Port Douglas, Queensland, (2002).
[17] S. Shirayama, ''Flow past a sphere: Topological transitions in the vorticity field,'' AIAA J. **30**, 349 (1992).
[18] T. A. Johnson and V. C. Patel, ''Flow past a sphere up to a Reynolds number of 300,'' J. Fluid Mech. **378**, 19 (1999).
[19] W. Z. Shen and T. P. Loc, ''Numerical method for unsteady 3D Navier–Stokes equations in velocity-vorticity form,'' Comput. Fluids **26**, 193 (1997).
[20] S. K. Aliabadi and T. E. Tezduyar, ''Parallel fluid dynamics computations in aerospace applications,'' Int. J. Numer. Methods Fluids **21**, 783 (1995).
[21] V. Kalro and T. Tezduyan, ''3D computation of unsteady flow past a sphere with a parallel finite element method,'' Comput. Methods Appl. Mech. Eng. **151**, 267 (1998).
[22] S. Mansoorzadeh, C. C. Pain, C. R. E. Oliveira, and A. J. H. Goddard, ''Finite element simulations of flow past a heated/cooled sphere,'' Int. J. Numer. Methods Fluids **28**, 903 (1998).
[23] R. Mittal, ''Planar symmetry in the unsteady wake of a sphere,'' AIAA J. **37**, 388 (1999).
[24] R. Mittal, ''A Fourier–Chebyshev spectral collocation method for simulating flows past spheres and spheroids,'' Int. J. Numer. Methods Fluids **30**, 921 (1999).
[25] R. Mittal and F. M. Najjar, ''Vortex dynamics in the shere wake,'' AIAA Pap. 99-3806 (1999).
[26] A. G. Tomboulides, S. A. Orszag, and G. E. Karniakidis, ''Direct and large-eddy simulations of axisymmetric wakes,'' AIAA Pap. 93-0546 (1993).
[27] A. G. Tomboulides and S. A. Orszag, ''Numerical investigation of transitional and weak turbulent flow past a sphere,'' J. Fluid Mech. **416**, 45 (2000).
[28] D. Kim and H. Choi, ''Large eddy simulation of turbulent flow over a sphere using an immersed boundary method,'' *Third AFSOR International Conference on Direct Numerical Simulations and Large Eddy Simulations* (University of Texas, Arlington, Texas, 2001).
[29] V. Seidl, S. Muzaferija, and M. Peric, ''Parallel DNS with local grid refinement,'' Appl. Sci. Res. **59**, 379 (1998).
[30] M. Schmid, ''Grobstruktursimulation turbulenter Strommungen auf unstrukturierten Gittern mit einer parallelen Finite-Volumen Methode,'' Ph.D. thesis, TUHH Hamburg, Germany (2001).
[31] I. Hadzic, V. Bakic, and M. Peric, ''Numerical and experimental analysis of flow around sphere at subcritical Reynolds number,'' 10-STAB Workshop, Gottingen, Germany (2001).
[32] D. Drikakis, ''Development and implementation of parallel high-resolution schemes in 3D flows over bluff bodies,'' *Parallel CFD Conference Implementation and Results Using Parallel Computers* (Elsevier, New York, 1995), p. 191.
[33] W. Koschel, M. Lotzerich, and A. Vornberger, ''Solution on unstructured grids for the Euler and Navier–Stokes equations,'' AGARD Conf. Proc. **437**, 26 (1988).
[34] G. S. Constantinescu and K. D. Squires, ''Role of turbulence model in prediction of turbulent flow over a sphere,'' ASME Paper FEDSM2000-11217 (2000).
[35] P. R. Spalart and S. R. Allmaras, ''A one-equation turbulence model for aerodynamic flows,'' Rech. Aerosp. **1**, 5 (1994).
[36] M. L. Shur, P. R. Spalart, M. K. Strelets, and A. K. Travin, ''Detached-eddy simulation of an airfoil at high angle of attack,'' Fourth International Symposium on Engineering Turbulence Modeling and Measurements, Corsica, France (1999).

Downloaded 19 Jul 2004 to 195.83.232.39. Redistribution subject to AIP license or copyright, see http://pof.aip.org/pof/copyright.jsp

[37]G. S. Constantinescu and V. C. Patel, ''A numerical model for simulation of pump-intake flow and vortices,'' J. Hydraul. Eng. **124**, 123 (1998).
[38]A. Travin, M. Shur, M. Strelets, and P. R. Spalart, ''Physical and numerical upgrades in the detached-eddy simulations of complex turbulent flows,'' Euromech Colloquium on LES and complex transitional and turbulent flows, Munich, Germany (2000b).
[39]F. M. Najjar and S. Balachandar, ''Low-frequency unsteadiness in the wake of a normal flat plate,'' J. Fluid Mech. **370**, 101 (1998).
[40]J. Jeong and F. Hussain, ''On the identification of a vortex,'' J. Fluid Mech. **285**, 69 (1995).

Downloaded 19 Jul 2004 to 195.83.232.39. Redistribution subject to AIP license or copyright, see http://pof.aip.org/pof/copyright.jsp